

Department of Physics and Astronomy
Heidelberg University

Bachelor Thesis in Physics
submitted by

Marta Fuentes Zamoro

born in Madrid (Spain)

2022

Measurement of the branching ratio of $D^0 \rightarrow K^- \pi^+ \mu^+ \mu^-$

This Bachelor Thesis has been carried out by Marta Fuentes Zamoro at the
Physikalisches Institut in Heidelberg
under the supervision of
Prof. Ulrich Uwer

Abstract

This bachelor thesis is dedicated to the study of the decay $D^0 \rightarrow K^- \pi^+ \mu^+ \mu^-$, analysing data collected with the LHCb detector during the years 2017-2018, corresponding to an integrated luminosity of 3.8 fb^{-1} . Decay candidates with the muon pair's invariant mass in the range $675\text{-}875 \text{ MeV}/c^2$ are considered. This region corresponds to the mass range of the $\rho^0 - \omega$ resonance. A value of the branching ratio is measured to be:

$$\mathcal{BR}(D^0 \rightarrow K^- \pi^+ \mu^+ \mu^-) = (5.70 \pm 0.09 \text{ (stat.)} \pm 0.42 \text{ (syst.)}) \times 10^{-6}$$

The decay $D^0 \rightarrow K^- \pi^+ \pi^+ \pi^-$ is used as normalisation channel.

Zusammenfassung

Diese Bachelorarbeit untersucht den Zerfall $D^0 \rightarrow K^- \pi^+ \mu^+ \mu^-$, indem Daten des LHCb-Detektor der Jahre 2017-2018 analysiert werden, was einer integrierten Luminosität von 3.8 fb^{-1} entspricht. Zerfallskandidaten der Ruhemasse des Myonenpaares im Bereich $675\text{-}875 \text{ MeV}/c^2$ werden betrachtet. Dieser Bereich entspricht der Masse der $\rho^0 - \omega$ Resonanz. Der bestimmte Wert des Verzweigungsverhältnisses ist:

$$\mathcal{BR}(D^0 \rightarrow K^- \pi^+ \mu^+ \mu^-) = (5.70 \pm 0.09 \text{ (stat.)} \pm 0.42 \text{ (syst.)}) \times 10^{-6}$$

Der Zerfall $D^0 \rightarrow K^- \pi^+ \pi^+ \pi^-$ wird als Normalisierungskanal benutzt.

Resumen

Este Trabajo de Fin de Grado está dedicado al estudio de la desintegración $D^0 \rightarrow K^- \pi^+ \mu^+ \mu^-$, analizando datos recogidos en el detector LHCb durante los años 2017-2018 correspondiente a una luminosidad integrada de 3.8 fb^{-1} . Se consideran los candidatos de la desintegración con una masa invariante de los dos muones en el rango $675\text{-}875 \text{ MeV}/c^2$. Esta región se corresponde al rango de masa de la resonancia $\rho^0 - \omega$. Se obtiene el siguiente valor para la razón de ramificación:

$$\mathcal{BR}(D^0 \rightarrow K^- \pi^+ \mu^+ \mu^-) = (5,70 \pm 0,09 \text{ (stat.)} \pm 0,42 \text{ (syst.)}) \times 10^{-6}$$

Para ello se emplea la desintegración $D^0 \rightarrow K^- \pi^+ \pi^+ \pi^-$ como canal de normalización.

Contents

1	Introduction	1
2	Theoretical background	2
2.1	The Standard Model	2
2.2	Decay $D^0 \rightarrow K^- \pi^+ \mu^+ \mu^-$	4
3	The LHCb experiment	7
3.1	Tracking system	7
3.2	Particle identification (PID) system	8
3.3	Trigger system	9
3.3.1	L0 trigger	9
3.3.2	High level trigger (HLT)	9
4	Event selection	11
4.1	Selection criteria	11
4.2	Efficiency calculation	17
5	Invariant mass fit	19
5.1	Branching ratio	24
6	Conclusions	26
A	Evolution of the events sample with the different cuts	29
A.1	Data sample	29
A.2	Signal simulation sample	30
A.3	Normalisation simulation sample	31

1 Introduction

Ever since the Standard Model (SM) was proposed, experiments have been carried out to test it and obtain the parameters involved in its description, such as coupling constants. Even though the theory has proved to be correct so far, it fails to explain questions like the matter-antimatter asymmetry of the universe. Therefore, the Standard Model cannot be complete as for now. Searches for New Physics that try to give an answer to these holes can be direct (production of new particles in an accelerator, for example) or indirect (signs of new particles or interactions in loop processes).

The LHCb detector at CERN was initially designed to perform indirect searches for New Physics in hadrons with bottom b quarks. Recently, the search has also been expanded to hadrons accommodating charm c quarks. The study of rare charm decays is interesting because it allows exploring Flavour Changing Neutral Currents [1](FCNC, see [2]) in the transition $c \rightarrow u$, which is not possible in B-Physics (dedicated to the study of B mesons, which contain a b quark). In general, new and unknown particles and interactions might modify the rate of a specific process, thus indirectly pointing towards the existence of New Physics (manifested via undiscovered particles, for instance).

This thesis focuses on the study of the branching ratio of the decay $D^0 \rightarrow K^- \pi^+ \mu^+ \mu^-$ ¹ using the normalisation channel $D^0 \rightarrow K^- \pi^+ \pi^+ \pi^-$ due to its similar characteristics. A precise value of this parameter will enable the study of other decays using this channel as normalisation. Among these processes, other charm decay modes such as $D^0 \rightarrow K^- K^+ \mu^+ \mu^-$ and $D^0 \rightarrow \pi^- \pi^+ \mu^+ \mu^-$ [3] are included. The decay studied in this thesis can be used as normalisation channel for the search of lepton flavour violating (LFV) decays (for instance $D^0 \rightarrow h^- h^+ \mu^\pm e^\mp$, where $h = K, \pi$) [4].

This thesis is structured as follows. Firstly, a brief introduction to the theoretical background is given in Sect. 2, while the detector system (LHCb) is explained in Sect. 3. Section 4 describes the selection done on the different event samples by applying adequate cuts. Afterwards, the efficiencies of these cuts are determined using the Monte-Carlo samples for both decay channels, while simultaneously fitting (Sect. 5) the final mass distribution. The branching ratio is calculated using the parameters obtained in the previous steps. Finally, the results are summarised and concluded in Sect. 6.

¹Unless otherwise stated, charge conjugation is assumed. Therefore, the decay $\overline{D}^0 \rightarrow K^+ \pi^- \mu^+ \mu^-$ is also considered.

2 Theoretical background

2.1 The Standard Model

The Standard Model (SM) [2] is the most accurate theory that describes the constituent blocks of nature and the forces that act between them. It is composed of twelve fermions (particles with half-integer spin, in this case spin 1/2 particles), which are divided into six quarks and six leptons (and their corresponding antiparticles); as well as four gauge bosons (particles with integer spin, spin 1 for these bosons), which are the mediators of the fundamental forces. An additional spin 0 boson, the Higgs boson, is required to explain the mass of particles.

Regarding the fermions, they are split into three generations with similar characteristics but different masses, each containing two quarks, a charged lepton and the associated neutrino. Additionally, quarks are grouped into two sectors: the up-type quarks (u, c, t) have an electric charge² of $+2/3$, while the down-type quarks (d, s, b) are characterised by an electric charge of $-1/3$. Leptons are classified considering their electric charge in charged leptons (e^-, μ^-, τ^-) and neutrinos (ν_e, ν_μ, ν_τ). While the latter are massless in the SM³, the former exhibit considerable differences in masses between generations. A summary of the quarks and leptons that form the Standard Model is given in Tables 1 and 2.

Generation	Quark	Charge (e)	Mass (MeV/ c^2)
First generation	up (u)	$+2/3$	2.16
	down(d)	$-1/3$	4.67
Second generation	charm (c)	$+2/3$	1.27×10^3
	strange (s)	$-1/3$	93.4
Third generation	top (t)	$+2/3$	172.69×10^3
	bottom (b)	$-1/3$	4.18×10^3

Table 1: Quarks in the Standard Model. Their electric charge and mass values are extracted from the Particle Data Group (PDG) [6].

Concerning the fundamental interactions [2], there are four of them (electromagnetic, weak, strong and gravity); however only three are explained within the framework of the Standard Model. While the electromagnetic interaction is mediated by the photon and only acts on particles that carry electric charge (quarks and charged leptons), the weak force is responsible for changing the flavour (type of particle) of particles with weak isospin (all fermions). Its corresponding gauge bosons W^\pm couple only to left-handed (LH) chiral particles and right-handed (RH) chiral antiparticles. Furthermore, the electromagnetic and weak forces were unified, leading to the electroweak interaction; which is also mediated by the Z boson. The

²It is measured in units of the fundamental electric charge e .

³The observation of neutrino oscillations shows that they have mass. Upper limits on their masses have been measured [5].

strong force is mediated by eight gluons g and acts only on particles with colour charge (quarks and gluons themselves). The last fundamental force is gravitation, which is not described by the SM. Additionally, the Higgs boson explains the mass of particles as a consequence of the coupling of fermions and bosons to the Higgs.

Generation	Lepton	Charge (e)	Mass (MeV/c^2)
First generation	electron (e^-)	-1	0.511
	electron neutrino (ν_e)	0	-
Second generation	muon (μ^-)	-1	105.7
	muon neutrino (ν_μ)	0	-
Third generation	tau (τ^-)	-1	1776.9
	tau neutrino (ν_τ)	0	-

Table 2: Leptons in the Standard Model. Their electric charge and mass values are extracted from the Particle Data Group (PDG) [6].

Due to the strong force, quarks can only be seen in colour neutral composites named hadrons. Depending on their quark content, hadrons are classified as baryons (containing three quarks $q_0q_1q_2$) or mesons (quark-antiquark $q_0\bar{q}_1$). Other composites having a bigger number of quarks (tetraquarks and pentaquarks) have been observed with LHCb [7].

Interaction	Boson	Charge (e)	Mass (GeV/c^2)
Electromagnetic	photon (γ)	0	$< 1 \times 10^{-27}$
	W	± 1	80.38
Weak interaction	Z	0	91.19
	Strong	gluon (g)	-
-	Higgs H	0	125.25

Table 3: Gauge bosons and the interactions they mediate. The values of their masses and charge are extracted from the Particle Data Group (PDG) [6].

Table 4 gives a summary of the mesons involved in the decay analysed in this study.

Particle name	Symbol	Quark content	Mass (MeV/c^2)
D* meson	D^{*+}	$c\bar{d}$	2010.26
D meson	D^0	$c\bar{u}$	1864.84
Kaon	K^-	$s\bar{u}$	493.68
Pion	π^+	$u\bar{d}$	139.57

Table 4: Mesons that appear in this study, along with their quark content and their mass, extracted from the Particle Data Group (PDG) [6]

2.2 Decay $D^0 \rightarrow K^- \pi^+ \mu^+ \mu^-$

The decay under study is part of the decay $D^{*+} \rightarrow D^0 (\rightarrow K^- \pi^+ \mu^+ \mu^-) \pi_s^+$, where D^0 and a slow pion (named as such due to its low momentum) are the daughter particles. A pictorial representation of the full decay is given in Fig. 1.

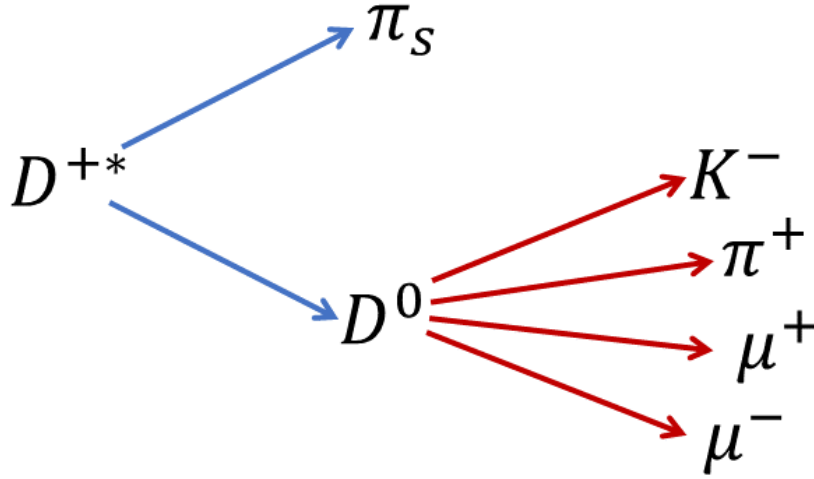
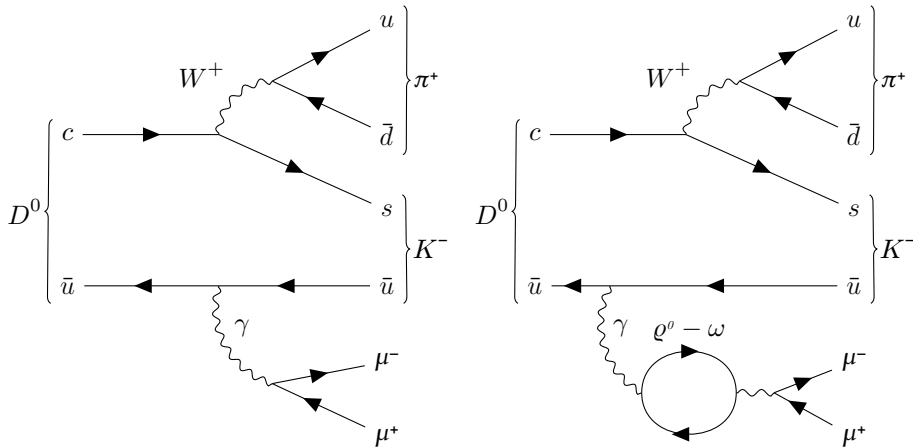


Figure 1: Schematic diagram of the decay studied in this process. The D^{*+} decays into a slow pion π_s^+ and a meson D^0 , which later experiences a 4-body decay into K^-, π^+, μ^+, μ^- . The particles that leave a signal are the slow pion as well as the daughter particles of the D^0 .

The decay $D^0 \rightarrow K^- \pi^+ \mu^+ \mu^-$ involves the weak interaction, as there exists a change in the quark flavour. Additionally, the muon pair can be produced directly (short distance decay) or via a resonance (long distance decay). The dimuon mass (invariant mass of the pair of muons) range employed in this thesis is $675 < m_{\mu\mu} < 875 \text{ MeV}/c^2$, which corresponds to the resonance $\rho^0 - \omega$. The Feynman diagrams at tree level for both possibilities are shown below. The diagram on the left belongs to the short distance contribution, whereas the one on the right represents the decay via resonance (long distance).



In order to study the branching ratio⁴, the normalisation channel $D^0 \rightarrow K^- \pi^+ \pi^+ \pi^-$ is used

⁴The branching ratio is defined as the fraction of particles that decay following an specific decay mode with respect to the total number of particles that decay following all possible modes.

because it is a well investigated decay whose branching ratio was obtained by the CLEO experiment [8] and is known to be $\mathcal{BR} = (8.287 \pm 0.043 \text{ (stat.)} \pm 0.200 \text{ (syst.)}) \times 10^{-2}$. As it is also a 4-body decay of the D^0 , kinematics are expected to be similar between both decays. It constitutes one of the biggest contributions to background in the decay studied, as pions can be misidentified as muons. Taking the normalisation channel into account, the branching ratio is calculated using Eq. (1), where \mathcal{BR} stands for branching ratio, ε represents the detection and selection efficiency and N is the number of event candidates for the corresponding decay.

$$\mathcal{BR} \left(D^0 \rightarrow K^- \pi^+ \mu^+ \mu^- \right) = \mathcal{BR} \left(D^0 \rightarrow K^- \pi^+ \pi^+ \pi^- \right) \cdot \frac{N_{D^0 \rightarrow K^- \pi^+ \mu^+ \mu^-}}{N_{D^0 \rightarrow K^- \pi^+ \pi^+ \pi^-}} \cdot \frac{\varepsilon_{D^0 \rightarrow K^- \pi^+ \pi^+ \pi^-}}{\varepsilon_{D^0 \rightarrow K^- \pi^+ \mu^+ \mu^-}} \quad (1)$$

The total efficiency for any decay is obtained according to Eq. (2). $\varepsilon_{acc \ \& \ rec}$ represents the acceptance and reconstruction efficiency, which accounts for the production of the event within the LHCb pseudorapidity⁵ η range (see Sect. 3) and the reconstruction as $D^0 \rightarrow K^- \pi^+ \mu^+ \mu^-$. $\varepsilon_{Trigger}$ stands for trigger efficiency; whereas ε_{selec} and ε_{PID} are selection and particle identification efficiencies. A detailed explanation on what each efficiency represents is given in Sect. 4.

$$\varepsilon = \varepsilon_{acc \ \& \ rec} \cdot \varepsilon_{Trigger} \cdot \varepsilon_{selec} \cdot \varepsilon_{PID} \quad (2)$$

Lastly, each individual efficiency is derived from Eq.(3). $nBefore$ and $nAfter$ represent the number of events before and after, respectively, a concrete selection requirement is applied.

$$\varepsilon = \frac{nAfter}{nBefore} \quad (3)$$

Efficiencies are calculated with respect to the previous step in the selection. The number of events N is extracted from a fit to the mass distribution (see Sect. 5). The idea behind calculating the branching ratio following Eq.(1) is to obtain a precise value by comparing the studied channel with a normalisation mode with similar features. This method reduces systematic uncertainties present in both decays. Additionally, the number of produced D^0 events is unknown, thus the branching ratio can only be determined via a normalisation channel.

A value for the branching ratio of the decay $D^0 \rightarrow K^- \pi^+ \mu^+ \mu^-$ has been obtained, both theoretically [9] and experimentally [10] (see Table 5). The difference between both values relies on the fact that the experimental measurement has been performed in the resonant region of the mesons ρ^0 and ω ($675 < m_{\mu\mu} < 875 \text{ MeV}/c^2$). In this region long distance contributions (coming from resonances) dominate. The theoretical value is obtained in the full dimuon mass spectrum. An upper limit of the branching ratio was previously set by the E791 collaboration [11]. It was concluded that the $\mathcal{BR} < 35.9 \times 10^{-5}$ at a 90% confidence level (CL).

⁵Pseudorapidity [2] is defined as $\eta = -\ln\left(\tan\left(\frac{\theta}{2}\right)\right)$, where θ is the angle measured from the beam line. It is Lorentz invariant and valid for the regime where the jet masses can be neglected (high-energy limit). The number of particles in each η region (defined by integer numbers) is constant.

Theoretical prediction [9]	6.7×10^{-6}
Experimental measurement [10]	$(4.17 \pm 0.12 \text{ (stat)} \pm 0.40 \text{ (syst)}) \times 10^{-6}$

Table 5: Theoretical prediction and experimental measurement of the branching ratio of the decay $D^0 \rightarrow K^- \pi^+ \mu^+ \mu^-$.

3 The LHCb experiment

The LHC (Large Hadron Collider) is a proton-proton pp circular accelerator located at CERN (Conseil Européen pour la Recherche Nucléaire, Geneva, Switzerland). The four main detectors are LHCb, ATLAS, CMS and ALICE, each of them located at a different interaction point. The objective of the LHCb detector [12] is to study heavy flavour hadrons (containing c and b quarks, as the t quark decays before it hadronises). LHCb is designed as a single-arm forward spectrometer of 20 meters in length, which covers the pseudorapidity range $2 < \eta < 5$. It consists of a series of silicon detectors, a magnet, two ring-imaging Cherenkov (RICH) detectors, two calorimeters and five muon stations. A diagram of the different constituents can be seen in Fig. 2.

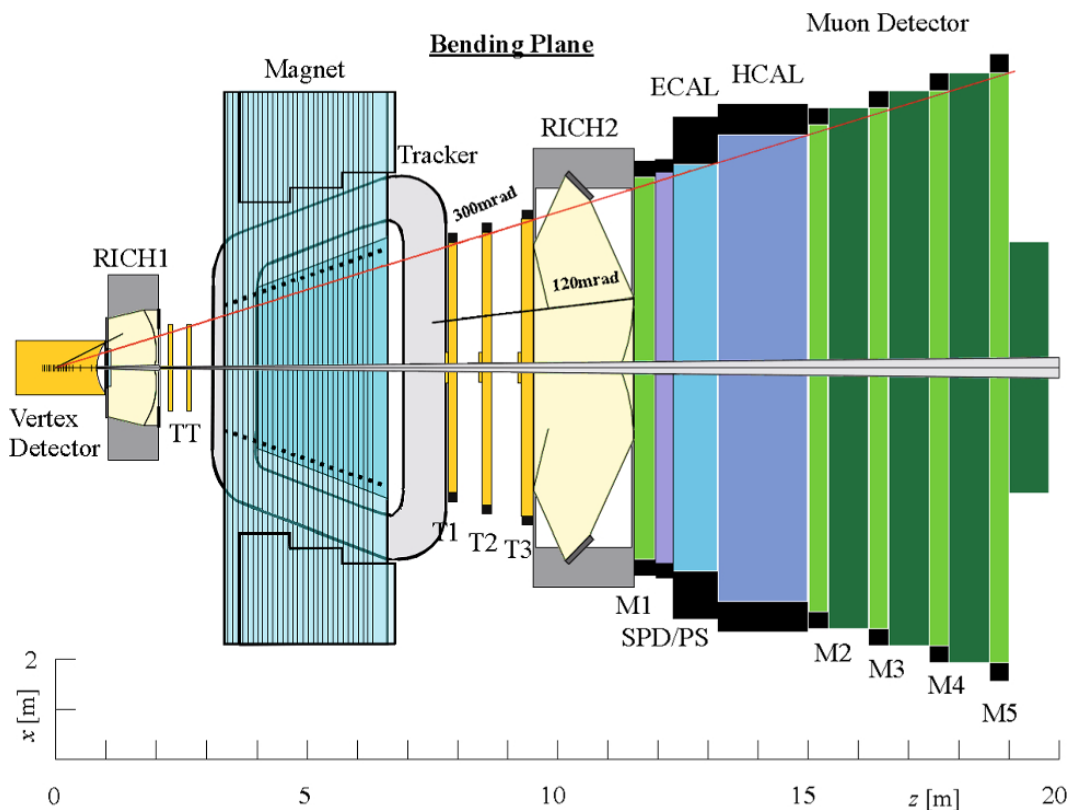


Figure 2: Top view of the LHCb detector extracted from [12].

3.1 Tracking system

In order to reconstruct the tracks of the produced particles, LHCb employs different high-precision tracking subdetectors. Firstly, the VERTex LOcator (VELO) is a silicon-strip detector, which is the closest to the interaction point. It is used to reconstruct the production points and decay vertices of hadrons. Additionally, a precision measurement of the impact parameter (IP)⁶ of all tracks relative to the primary vertex (PV)⁷, as well as the lifetime of the hadrons, is performed. It is split into two halves, which are positioned only after the LHC beam is stable so as to avoid infringing damage to the detector.

⁶Minimum distance from a concrete point to the projected trajectory of the initial particle before the decay.

⁷Defined as the point where the proton-proton collision takes place.

Furthermore, there exist four planar tracking stations, one of them, the TT (Tracker Turicensis) station, located between the RICH1 (Ring Imaging Cherenkov, see Sect. 3.2) and the magnet; and the other three, T1, T2 and T3 located downstream (after) of the magnet. The TT detector is formed by four stations consisting of silicon microstrip planar modules. The T1-T3 tracking stations are divided into two parts. The Inner Tracker (IT) surrounds the beam and is a silicon strip detector, whereas the Outer Tracker (OT) is a gaseous detector.

The magnet employed to deflect charged particles (and therefore measure their momenta) has an integrated field of 4 T·m and is located between the TT and T1 tracking stations. At LHCb, data is collected for both polarities of the magnet.

3.2 Particle identification (PID) system

The precise identification of the different particles is essential to the analyses that are within the scope of LHCb. Consequently, there are several components that contribute to it. The discrimination between π , K and p is done using two Ring Imaging Cherenkov detectors (RICH), which are based on Cherenkov radiation. The first one, RICH1, is located upstream (before) of the magnet and differentiates particles in the low momentum region. The RICH2 is located between T3 and the first muon station M1 and is responsible for identification in the high momentum region. The combination of momentum and Cherenkov angle is used to infer a value for the mass and thus indicate which particle it is.

Calorimeters represent the other fundamental part of the PID system and are responsible for the identification of hadrons, electrons and photons, as well as the measurement of their energies and positions for the hardware trigger (L0 trigger). The calorimeter system consists of a scintillator pad (SPD) and preshower (PS) detectors, an electromagnetic calorimeter (ECAL) and a hadronic calorimeter (HCAL).

Lastly, there are five muon stations, which are specialized in the detection of muons. The first station, M1, is located before the calorimeters and its main objective is to improve the measurement of the transverse momentum p_T ⁸ for the trigger system. The other four M2-M5 are interspersed with iron absorbers and are located after the calorimeters. In order to conclude that a concrete particle is a muon, tracks in the different tracking stations as well as a signal in the muon stations are asked for.

The probability distribution of a particle being a certain type of particle is a result of a combination of all the information collected by all detector parts and it is stored in variables named *ProbNN*.

⁸The transverse momentum is defined as $p_T = \sqrt{p_x^2 + p_y^2}$, where p_x and p_y represent the momentum of the particle in the plane perpendicular to the beam.

3.3 Trigger system

The selection of events is performed by a trigger system, which allows achieving a high efficiency in such selection while simultaneously rejecting the majority of background events. It is composed of two major parts: L0 trigger and High level trigger.

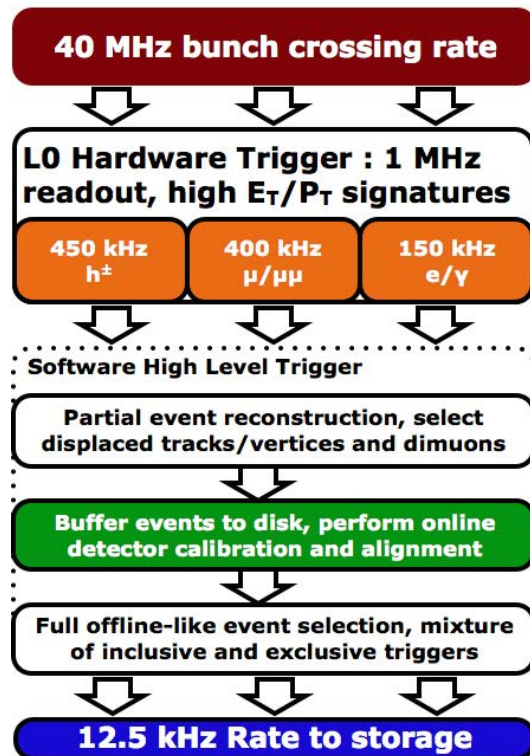


Figure 3: Trigger overview in Run 2, extracted from [13].

3.3.1 L0 trigger

Based on custom electronic boards, the L0 trigger (also named hardware trigger) is divided into three independent components. The L0-PileUp trigger is in charge of rejecting the multiple interactions that occur within one bunch crossing (known as pile-up). The L0-Calorimeter trigger extracts information from the calorimeter system and, using the transverse energy $E_T = E_0 \cos \theta$, classifies the particles into hadron, photon or electron candidates. Lastly, the L0-Muon trigger requires a hit in all five muon stations by the muon candidate. Applying all L0 triggers, the data output (see Fig.3) is reduced to 1 MHz.

In the concrete case of the decay $D^0 \rightarrow K^- \pi^+ \mu^+ \mu^-$, strict cuts on L0 Muon for both muons and L0 Hadron for the two involved mesons are applied.

3.3.2 High level trigger (HLT)

This part of the trigger system is applied in the Event Filter computer Farm (EFF) and is additionally separated into two different stages: HLT1 and HLT2. While the first one, HLT1, processes the full L0 data set and reduces the amount of data to approximately 110 KHz by doing a partial event reconstruction, the HLT2 line takes advantage of the already reduced data set from HLT1 to perform a full event reconstruction. The steps followed in the reconstruction are track reconstruction of charged particles and a posterior

particle identification.

After all trigger steps are applied, the rate is reduced to 12.5 kHz, which is stored and analysed afterwards.

To study the decay $D^0 \rightarrow K^- \pi^+ \mu^+ \mu^-$, the HLT1 trigger lines applied (Hlt1TrackMuonDecision and Hlt1TrackMVAMuonDecision) involve both muons, while the HLT2 line is the one specifically designed for the decay at hand.

The decay studied ($D^0 \rightarrow K^- \pi^+ \mu^+ \mu^-$) is reconstructed using information from different parts. The mesons K^- and π^+ leave signal in the HCAL and are distinguished using their signature in the RICH; whereas muons are mostly detected in the muon chambers. For all four particles, the magnet is essential to measure their momenta (different radii after deflection).

4 Event selection

Three different event samples have been used to perform this analysis. The data sample corresponds to the data taken with LHCb using pp collisions with a centre of mass energy of $\sqrt{s} = 13$ TeV for the years 2017 and 2018 and both polarities of the magnet. Additionally, simulation samples generated using Monte-Carlo are studied. These event samples reproduce the signal and normalisation channel. The decay mode $D^0 \rightarrow K^- \pi^+ \pi^+ \pi^-$ is used as selection normalisation channel. However, the events of this decay are selected as $D^0 \rightarrow K^- \pi^+ \mu^+ \mu^-$ events -i.e the two pions are wrongly identified as muons. The reason why it is done is purely technical: in LHCb all events need to be triggered and preselected by specific preselection and trigger lines. For the channel $D^0 \rightarrow K^- \pi^+ \pi^+ \pi^-$ there was no such trigger line. Therefore, only events which are wrongly identified as $K^- \pi^+ \mu^+ \mu^-$ are preselected. Consequently, the number of events in the Monte-Carlo sample for the normalisation channel is noticeably lower than in the case of the signal decay. Table 6 summarizes the number of events analysed.

	Data	Signal (Monte-Carlo)	Normalisation (Monte-Carlo)
Number of events	68976208	828107	83129

Table 6: Number of events before applying selection requirements for each event sample studied. The number of events in the normalisation Monte-Carlo is substantially smaller because the decay $D^0 \rightarrow K^- \pi^+ \mu^+ \mu^-$ is imposed during the reconstruction stage.

4.1 Selection criteria

In order to analyse the collected data, final state particles are combined to build signal candidates of the decay chain $D^{*+} \rightarrow D^0 (\rightarrow K^- \pi^+ \mu^+ \mu^-) \pi^+_s$ following a selection sequence. This selection is mainly aimed at removing background ($D^0 \rightarrow K^- \pi^+ \pi^+ \pi^-$ in this case, considered peaking background) and badly reconstructed decays. Moreover, requirements on the track kinematics and reconstruction quality are imposed to remove combinatorial background (coming from randomly associated tracks).

First of all, only tracks with at least one primary vertex (PV) are reconstructed. After this step, the four daughter particle candidates are asked to satisfy the criteria of having a transverse momentum higher than 300 MeV/ c , as well as a momentum superior to 3 GeV/ c in the case of hadrons and 4 GeV/ c for muons. Additionally, these particles must fulfil requirements on track quality (χ^2/dof (degree of freedom) < 3) and be inconsistent with coming from the primary vertex. Therefore a cut on the impact parameter IP $\chi^2 > 3$ is imposed. Tracks with a ghost probability inferior to 0.5 are selected, so as to reduce the inclusion of random ghost tracks reconstructed by the software. The PID conditions, based on the *ProbNN* variables, must be satisfied by candidate pions and kaons (*ProbNNhadron* > 0.7); whereas the corresponding ones for muons are implemented following the necessities that arise during fit, which lead to *ProbNNmuon* > 0.2 . A cut on the *isMuon* variable (true only for muons) is also applied to both muon candidates, in order to reduce the background stemming from the misidentification of pions as muons.

Once the four daughter particles are selected following the above mentioned conditions and provided they also satisfy the fact that the largest distance of closest approach to the D^0 (MAXDOCA) is lower than 0.3 mm and that the IP of at least one daughter particle is greater than 9 mm, they are added to form the D^0 , which is also required to fulfil some kinematic and vertex quality conditions. The (transverse) momentum of the D^0 candidate must be higher than (2.5) 3 GeV/c, thus further suppressing contributions from the combinatorial background. Additionally, the reconstructed mass of the D^0 is asked to lie between $1780 < m_{D^0} < 1950$ MeV/c², which leaves a margin of 85 MeV/c² on both sides (left and right) from the measured value (see Table 4). Furthermore, the D^0 candidate is asked to present a significant displacement from the PV, so it must have a flight distance⁹ $\chi^2 > 36$. The D^0 decay vertex must have a vertex $\chi^2/\text{dof} < 8$ to ensure good quality, as well as a restriction on the cosine of the direction angle¹⁰ (DIRA), which must be superior to 0.9999. Finally, a requirement on the IP $\chi^2 < 9$ is set, due to the fact that the D^0 comes from the primary vertex. By applying this cut, background from other decays is removed.

On another step, a slow pion candidate (coming from the decay of the D^{*+}) with transverse momentum higher than 120 MeV/c and good track quality (Track $\chi^2/\text{dof} < 3$) is combined with the D^0 to form a D^{*+} meson, whose transverse momentum must exceed 2 GeV/c and the difference between the masses of the D^{*+} and D^0 is limited to the range $120 < \Delta m < 200$ MeV/c². For this purpose, the variable obtained from the Decay Tree Fitter (DTF) is used. The DTF considers the vertex location (which has an impact on the parameter of the particle) and reconstructs the decay using all other parameters and calculates the mass. The DOCA of the daughter particles of the D^{*+} are required to be inferior to 0.3 mm and the D^{*+} vertex satisfies the minimal vertex quality condition (Vertex $\chi^2/\text{dof} < 20$).

In the selection procedure described above, the reconstruction is performed starting from the final detected particles and going backwards until the initial D^{*+} is reached. A summary of all selection cuts is given in Table 7.

As it was explained in Sect. 3 each event undergoes a trigger selection. In the case of the decay $D^0 \rightarrow K^- \pi^+ \mu^+ \mu^-$, a positive L0 trigger level decision is asked for muons and hadrons in such a way that a signal is detected for at least one of the four daughter particles. At HLT1, at least one of the muons is positively matched to the objects triggering either the Hlt1TrackMuonDecision or Hlt1TrackMVAMuonDecision. Both trigger lines are Trigger On Signal (TOS), which means that the particle whose data is saved is indeed the particle that caused the trigger. For the HLT2 level, a trigger cut specific to this charm decay is applied.

An additional cut on the dimuon mass range is applied, as this thesis focuses on the study of the branching ratio of $D^0 \rightarrow K^- \pi^+ \mu^+ \mu^-$ in the resonant spectrum of $\rho^0 - \omega$. Therefore,

⁹Defined as the distance from primary to secondary vertex.

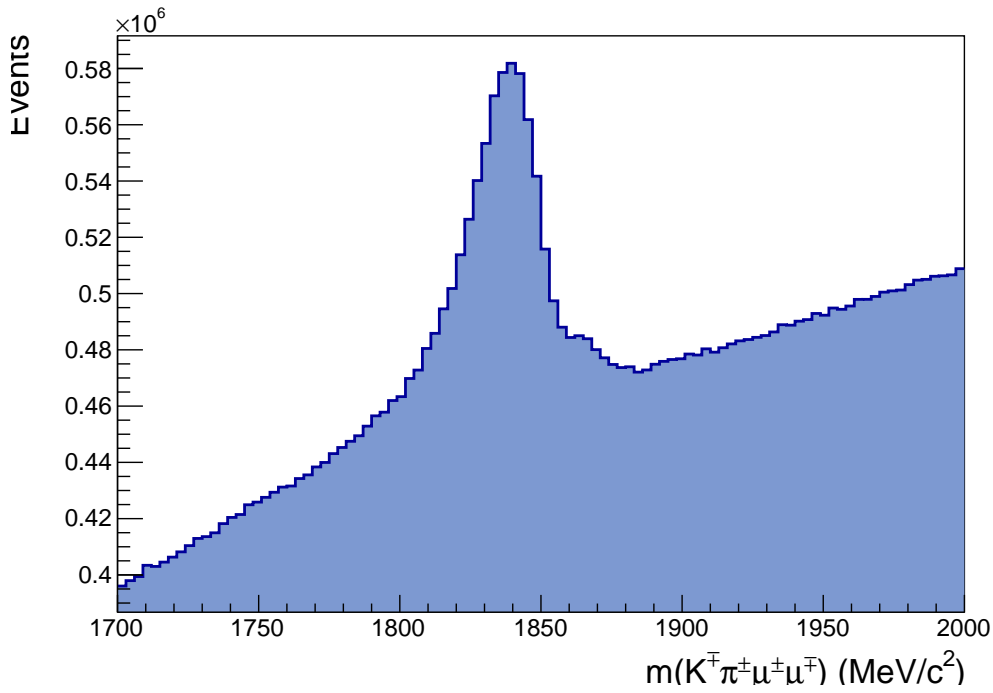
¹⁰The direction angle is defined as the angle between the momentum of the reconstructed intermediate particles with respect to the vector connecting the primary and secondary vertices.

the dimuon mass is limited to $675 < m_{\mu\mu} < 875 \text{ MeV}/c^2$. However, it should be considered that the branching fraction of the normalisation channel was measured without applying any restriction on the invariant mass of the pions that are misidentified as muons. This problem will be solved later during the fit (Sect. 5).

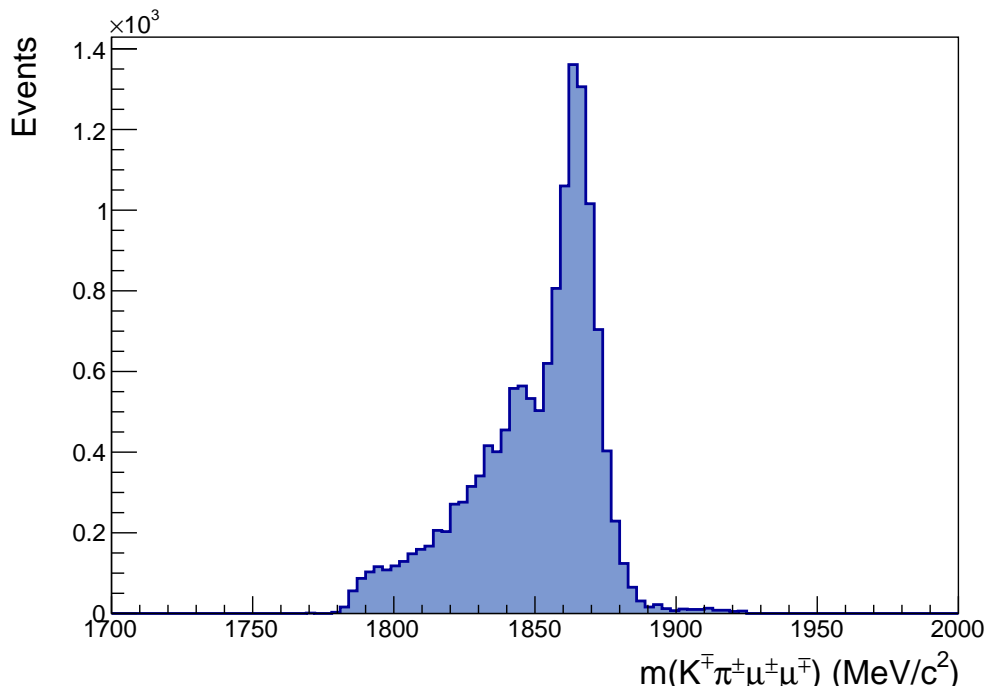
Particle	Variable	Requirement
K, π, μ	p_T	$> 300 \text{ MeV}/c$
	p	$> 3(4) \text{ GeV}/c$ for hadrons (muons)
	Impact parameter χ^2	> 3
	Track χ^2/dof	< 3
	ProbNNghost	< 0.5
K	ProbNNk	> 0.7
π	ProbNNpi	> 0.7
μ	isMuon	True
	nSharedMuon	0
D^0	p	$> 3 \text{ GeV}/c$
	p_T	$> 2.5 \text{ GeV}/c$
	$m(\text{DTF})$	$< 1780 \text{ MeV}/c^2$
		$> 1950 \text{ MeV}/c^2$
	Vertex χ^2/dof	< 8
	Flight distance χ^2	> 36
	Impact parameter χ^2	< 9
	Cosine of the direction angle	> 0.9999
	Largest distance of closest approach of daughters	$< 0.3 \text{ mm}$
Impact parameter χ^2 of at least one of the daughters	$> 9 \text{ mm}$	
D^{*+}	p_T	$> 2 \text{ GeV}/c$
	Vertex χ^2/dof	< 20
	Distance of closest approach of daughters (DOCA)	$< 0.3 \text{ mm}$
	$\Delta m(\text{DTF})$	$< 120 \text{ MeV}/c^2$
		$> 200 \text{ MeV}/c^2$
π_s	p_T	$> 120 \text{ MeV}/c$
	Track χ^2/dof	< 3
	Number of primary vertices	≥ 1

Table 7: Selection requirements implemented. Modified from [14] and [15].

Concerning the simulation event samples, the same conditions are required. In order to ensure that the correct decay is analysed, the particles in the simulation sample are matched to the studied decay.



(a) Data sample before any cut was applied.

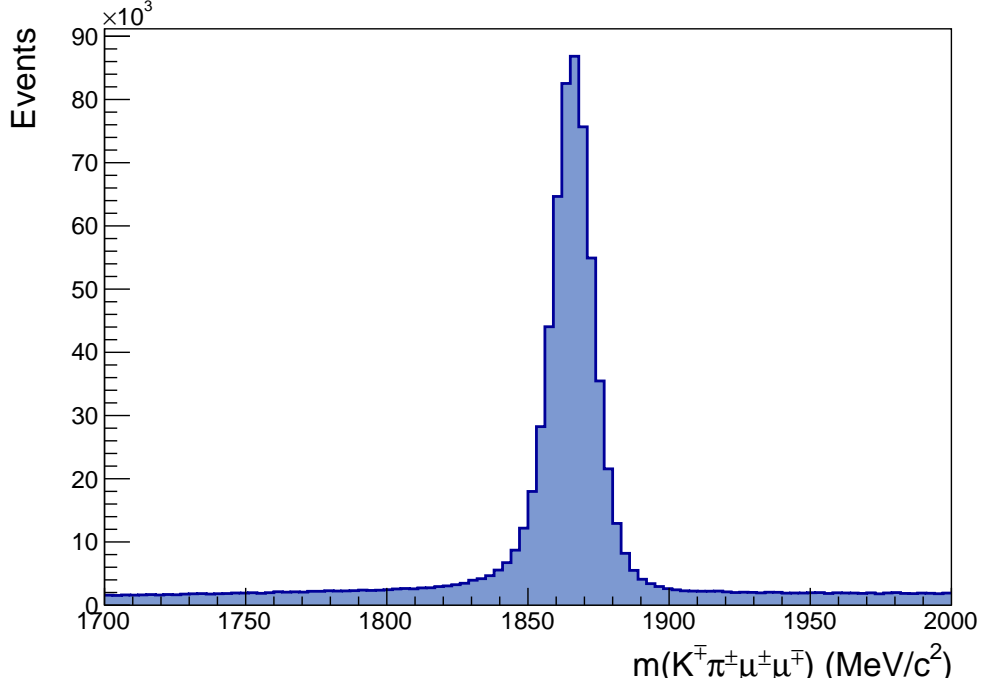


(b) Data sample after the cuts mentioned in the text are applied.

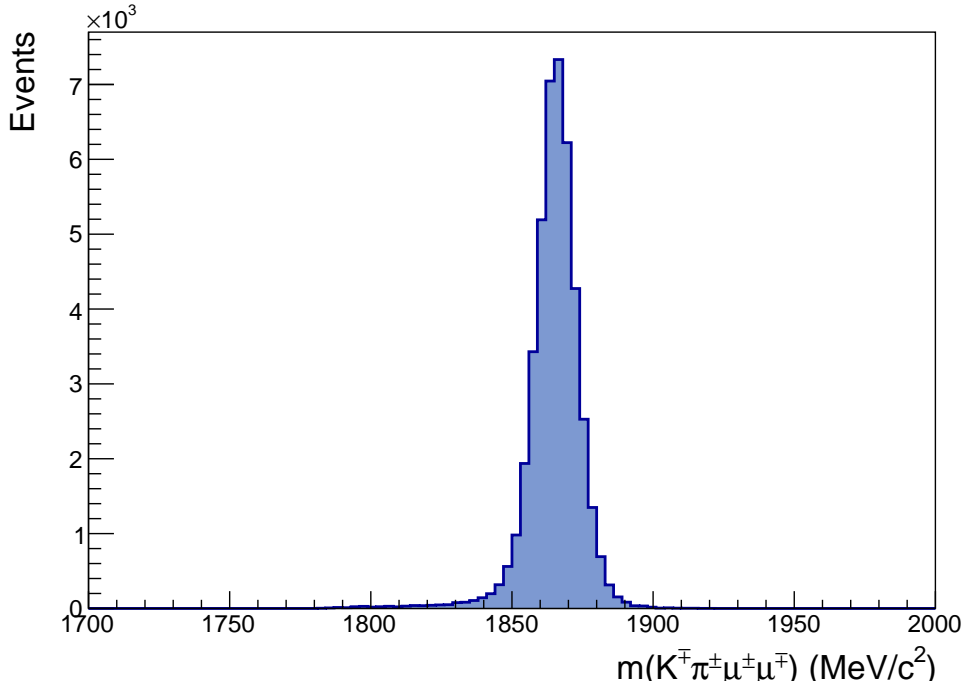
Figure 4: Evolution of the data sample after selection cuts are applied. It can be seen that both the peaking background (the peak is located at $1840 \text{ MeV}/c^2$ approximately) and the combinatorial background are drastically reduced, leaving a peak around $1860 \text{ MeV}/c^2$, which corresponds to the decay $D^0 \rightarrow K^- \pi^+ \mu^+ \mu^-$.

A comparison of the initial and selected (after all cuts are applied) data can be seen in Fig. 4. Before any selection criteria is applied, the data sample has a significant peak centred around $1840 \text{ MeV}/c^2$, which corresponds to the peaking background (decay $D^0 \rightarrow K^- \pi^+ \pi^+ \pi^-$). A small bump located approximately at $1860 \text{ MeV}/c^2$ (mass of the D^0) can be seen on top of the considerable background. These events belong to the decay $D^0 \rightarrow K^- \pi^+ \mu^+ \mu^-$. After the full selection procedure is performed, the majority of background is removed, thus leaving a

clear peak at $1860 \text{ MeV}/c^2$, which corresponds to the mass of the D^0 . The secondary peak to the left, located at $1840 \text{ MeV}/c^2$, corresponds to $D^0 \rightarrow K^- \pi^+ \pi^+ \pi^-$. The drastic reduction in the number of events of $D^0 \rightarrow K^- \pi^+ \pi^+ \pi^-$ is a consequence of the applied PID conditions. In summary, the decay to $K^- \pi^+ \pi^+ \pi^-$ is dominant before any selection has been done (peak located at $1840 \text{ MeV}/c^2$, see Fig. 4a). Afterwards, the decay to $K^- \pi^+ \mu^+ \mu^-$, which is slightly visible in the initial sample, becomes dominant (peak at $1860 \text{ MeV}/c^2$, see Fig. 4b).

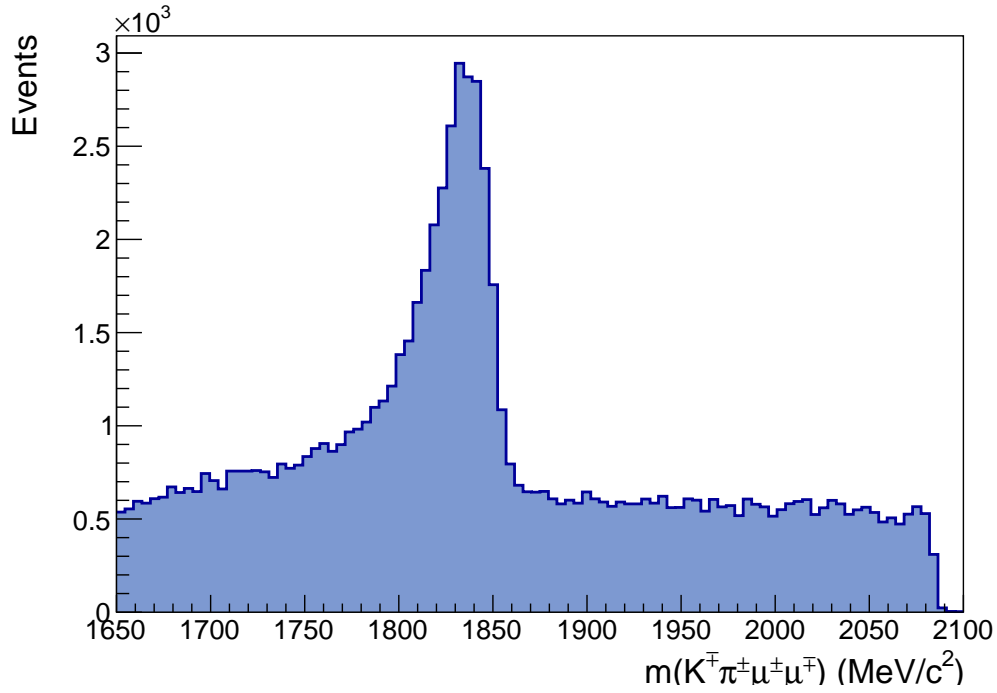


(a) Signal simulation event sample before any cut is applied.

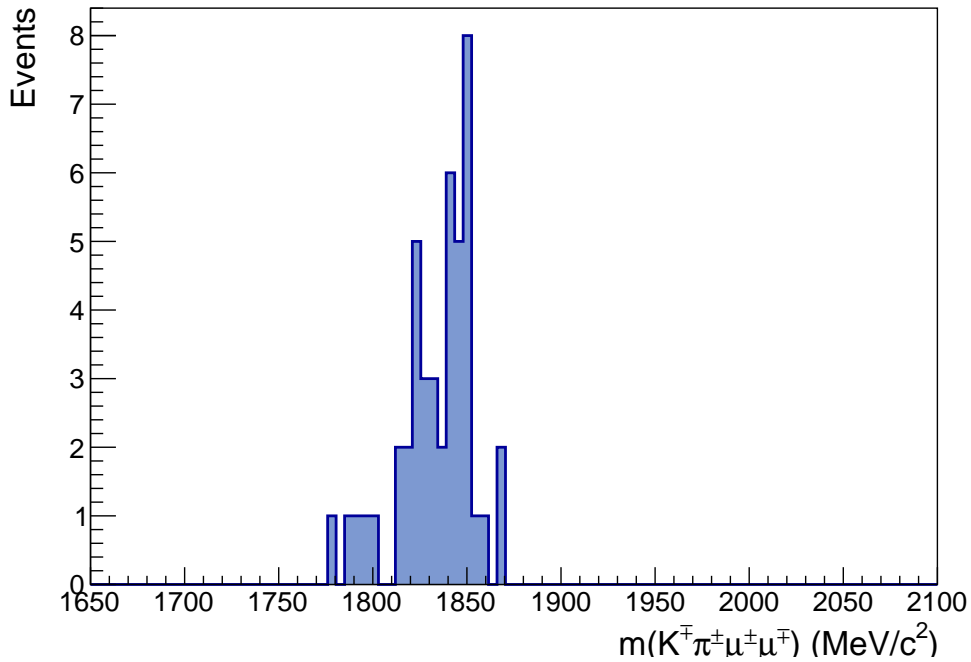


(b) Signal simulation event sample after the cuts mentioned in the text are applied.

Figure 5: Evolution of the signal simulation sample after selection cuts are applied. The shape and location of the peak do not change, which is to be expected. However, the combinatorial background stemming from wrongly identified signal events is removed and almost none is left.



(a) Normalisation simulation event sample before any cut is applied.



(b) Normalisation simulation event sample after the cuts mentioned in the text are applied.

Figure 6: Evolution of the normalisation simulation sample after selection cuts are applied. Almost all events are removed, which is a consequence of the fact that the cuts applied are designed to study the signal decay, so the wrong reconstruction of the pions as muons does pose a problem.

On the other hand, Figs. 5 and 6 show the evolution of the simulation samples for the signal decay and the normalisation mode, respectively. By applying the same cuts as to the data, information on the value of the efficiency can be extracted (the full procedure is explained in Sect. 4.2). In the case of the signal decay ($D^0 \rightarrow K^- \pi^+ \mu^+ \mu^-$), there is no major change neither on the location nor the shape of the signal after the cuts are applied. The peak is situated at approximately $1860 \text{ MeV}/c^2$, which explains the location of the principal peak in

Fig. 4b. In the selection procedure only combinatorial background is removed. This source of background arises from the fact that some particles which do not belong to the signal event are reconstructed as such. This behaviour is to be expected, as the cuts are designed to fit this decay.

In the case of the normalisation channel, performing the full selection drastically reduces the number of events because they are wrongly reconstructed as $K^- \pi^+ \mu^+ \mu^-$. Before any cut is applied, there is a peak located around $1840 \text{ MeV}/c^2$, which corresponds to the large peak seen in Fig. 4a, with a tail to the left and a bulk of combinatorial background. Once all conditions are set, almost no event survives, for the cuts applied are specifically designed for the signal decay.

The plots showing the evolution of the samples with the selection procedure can be seen in Appendix A.

4.2 Efficiency calculation

The ratio of efficiency for the signal and normalisation channel is fundamental to obtain the value of the branching ratio. Following expression (3), the efficiency for each applied cut is calculated, using for this purpose the Monte-Carlo simulated event samples. Instead of obtaining an individual value for each cut, the selection criteria are grouped by sections and a combined efficiency value is provided. The uncertainty is calculated using the binomial error, as the variables involved (n_{Before} and n_{After}) are correlated and follow a binomial distribution. As it was already mentioned above, the value of the branching ratio of the normalisation channel was measured using the full dimuon mass range. Consequently, the efficiencies related to the channel $D^0 \rightarrow K^- \pi^+ \pi^+ \pi^-$ are obtained without applying the selection criteria on the dimuon mass range, so that Eq.(1) is valid. On the contrary, the efficiencies belonging to the signal mode include the restriction of the dimuon mass. Table 8 collects the values for the combined efficiencies, as well as the overall efficiency, calculated considering Eq. (2); for both channels studied. The uncertainty associated to the overall efficiency is obtained performing an error propagation of the individual ones.

The first efficiency, named **acceptance and reconstruction as $D^0 \rightarrow K^- \pi^+ \mu^+ \mu^-$** $\varepsilon_{acc \ \& \ rec}$, accounts for the limited pseudorapidity acceptance range of the LHCb (it affects data and simulation events), as well as the generation and filter of the events in the proper Monte-Carlo software. It also considers the fact that the raw events undergo a prior reconstruction as $D^0 \rightarrow K^- \pi^+ \mu^+ \mu^-$, thus reducing the number of events. In the generation stage, the acceptance of the LHCb detector is considered for both signal and normalisation; whereas an additional cut on the transverse momentum of the slow pion π^+_s is applied only in the case of the decay $D^0 \rightarrow K^- \pi^+ \pi^+ \pi^-$ event sample. Furthermore, the filter requires a positive match in one of a series of HLT2 lines only for the normalisation mode, due to the fact that a wrong event signature is reconstructed. This condition is applied after the events are generated but before reconstruction takes place. The generation and filter cuts only exist

in Monte-Carlo and are employed to save computing power. As they are weaker than the other restrictions applied afterwards, they do not alter the overall value of the efficiency.

Concerning the **trigger** efficiency, $\varepsilon_{Trigger}$, it considers the reduction caused by the different stages in triggering (L0, HLT1 and HLT2 lines specified in Sect. 4.1) on the number of events studied.

According to the order specified by Eq.(2) the next efficiency in line is the **selection** efficiency, which groups all kinematic cuts collected in Table 7, as well as the applied cut on the mass range. Variables such as the momenta of the particles or the ones related to the vertex quality are included in this efficiency.

Finally, the **Particle Identification** efficiency, ε_{PID} , reflects the reduction produced by the PID selection conditions implemented. The PID efficiency of both decays (signal and normalisation) is noticeably different, although of the same order of magnitude. In the normalisation channel, the two misidentified pions are treated as muons and the same constraints as in the signal mode are applied. Consequently, the value for the normalisation channel is considerably lower than the one from the signal mode.

Summarising, the efficiencies for the normalisation channel are lower, being the acceptance and reconstruction and trigger stages the ones that lead to a considerable reduction in statistics. It must be noted that the values given in Table 8 are obtained when the specified order of cuts is followed. If a different order was to be imposed, the concrete values of the efficiencies would change but the overall one would not vary.

	Signal (%)	Normalisation (%)
Acceptance and reconstruction $\varepsilon_{acc \& rec}$	0.286 ± 0.003	$(2.19 \pm 0.03) \times 10^{-4}$
Trigger $\varepsilon_{Trigger}$	21.58 ± 0.07	6.2 ± 0.2
Selection ε_{selec}	77.5 ± 0.1	66.3 ± 1.5
Particle identification ε_{PID}	69.2 ± 0.2	19.7 ± 1.6
Overall efficiency ε	0.0331 ± 0.0004	$(1.8 \pm 0.2) \times 10^{-6}$

Table 8: Summary of the efficiencies of the different cuts applied for both the signal (with dimuon mass range) and the normalisation (without dimuon mass range) decays. The value of the overall efficiency is obtained using Eq. (2).

5 Invariant mass fit

The selected data samples are a mixture of signal and background candidates, which are separated by performing a fit to the invariant D^0 mass ($m(D^0)$). The fit model used consists of three components:

- Signal i.e. $D^0 \rightarrow K^- \pi^+ \mu^+ \mu^-$
- Peaking background i.e. $D^0 \rightarrow K^- \pi^+ \pi^+ \pi^-$
- Combinatorial background

The individual probability density functions (PDF) of the signal and peaking background are obtained from simulation samples, while the combinatorial PDF is extracted from the data sample. Due to the fact that two data samples (with and without dimuon mass range) are being dealt with, a simultaneous fit of both is done using the RooFit package [16] available in ROOT [17]. Additionally, the pull plot [18] of the fit is obtained. It is defined as the plot of the difference between curve and data points.

The first stage is to perform a fit to the simulation event samples with the same selection procedure as applied to data. Both the shape (PDF) and the corresponding parameters are extracted from this first fit and will later be used when the data sample is fitted. In the case of the signal channel, the PDF that best describes the data points is a sum of Johnson SU [19] and Bukin [18] PDFs (see Eqs. 4 and 5, respectively), where a parameter c is used to regulate the contribution from both PDFs.

$$PDF(\text{Johnson } SU) = \frac{\delta}{\lambda\sqrt{2\pi}} \cdot \frac{1}{\sqrt{1 + \left(\frac{x-\mu}{\lambda}\right)^2}} \cdot \exp\left(-\frac{1}{2} \cdot \left(\gamma + \delta \cdot \text{asin}\left(\frac{x-\mu}{\lambda}\right)\right)^2\right) \quad (4)$$

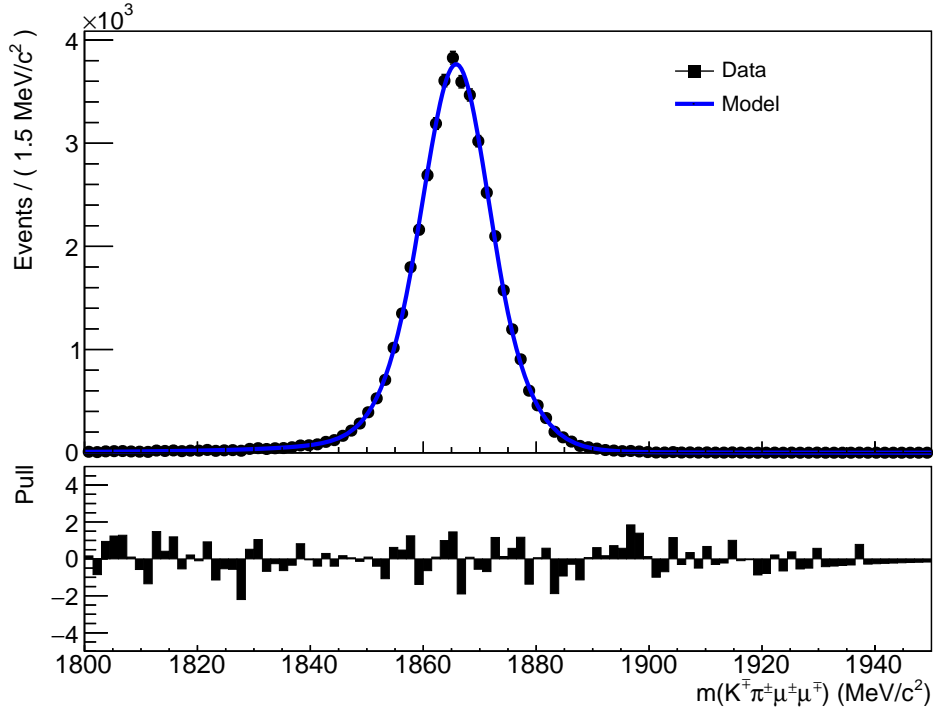
where x stands for the mass, μ represents the location of the Gaussian component, λ is the width of the Gaussian component, γ is a shape parameter that distorts the distribution to the left or right and δ is the shape parameter that determines the strength of the Gaussian-like component.

$$PDF(\text{Bukin}) = A_p \cdot \exp\left(\frac{\xi \cdot \sqrt{\xi^2 + 1} \cdot (x - x_1) \cdot \sqrt{2 \ln 2}}{\sigma_p \left(\sqrt{\xi^2 + 1} - \xi\right)^2 \cdot \ln\left(\sqrt{\xi^2 + 1} + \xi\right)} + \rho \cdot \left(\frac{x - x_i}{x_p - x_i}\right)^2 - \ln 2\right) \quad (5)$$

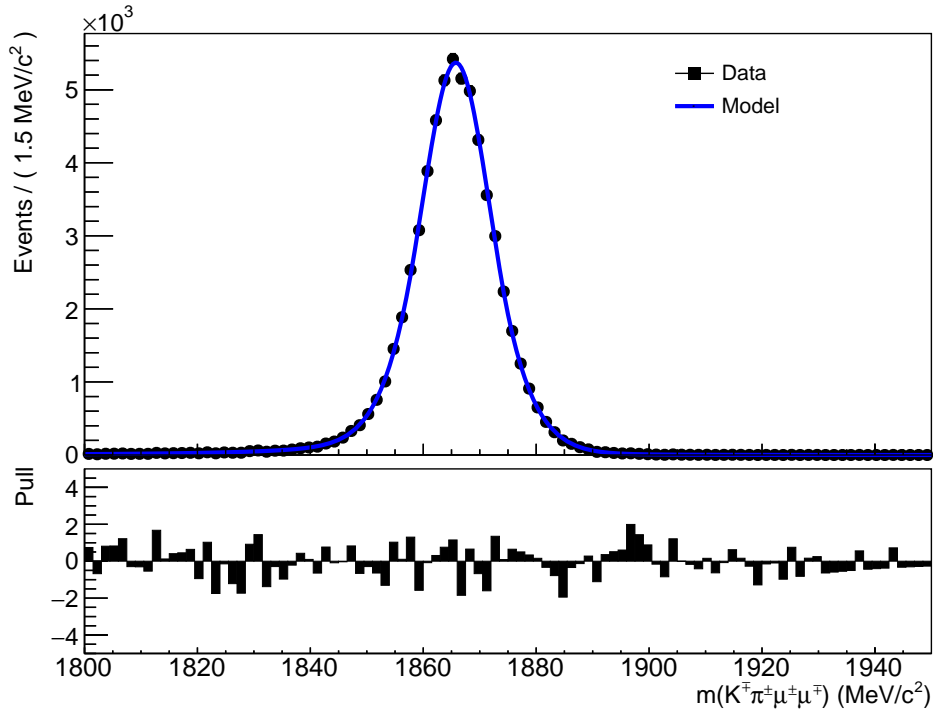
$$x_{1,2} = x_p + \sigma_p \cdot \sqrt{2 \ln 2} \cdot \left(\frac{\xi}{\sqrt{\xi^2 + 1}} \mp 1\right) \quad (6)$$

where x is the mass, x_p and σ_p stand for the peak position and width (Full Width Half Maximum/2.35) respectively; x_i represents the peak asymmetry and ρ_1 and ρ_2 parametrise the left and right tails. If $x < x_1$, $\rho = \rho_1$ and $x_i = x_1$, while $\rho = \rho_2$ and $x_i = x_2$ if $x \geq x_2$.

The result can be seen in Fig. 7, where not only the events with the dimuon mass range but also the ones without it are depicted.



(a) Fit with dimuon mass range cut.



(b) Fit without dimuon mass range cut.

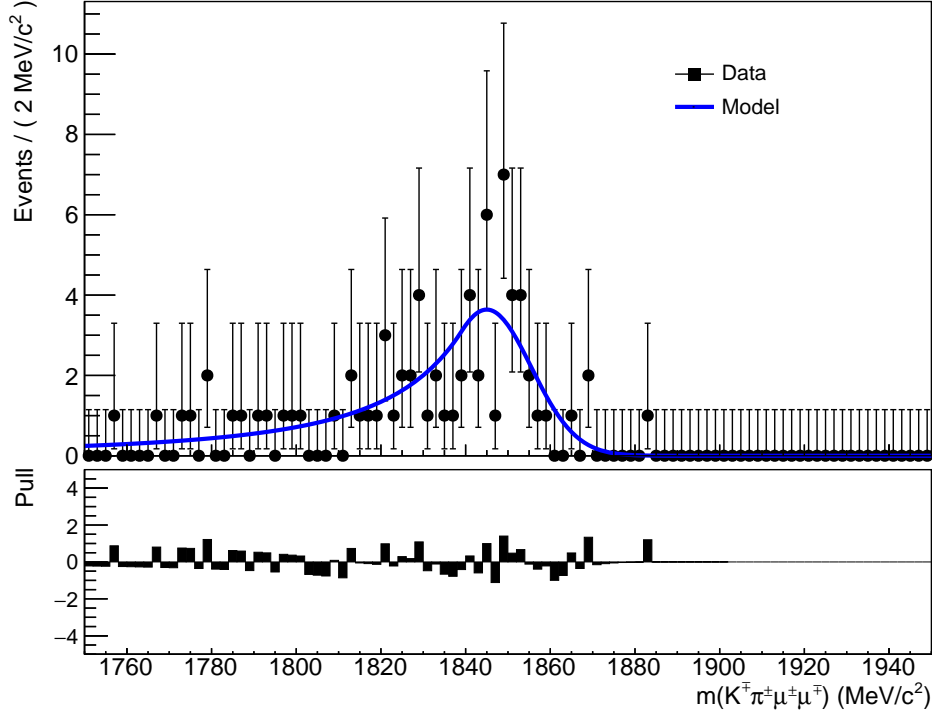
Figure 7: Fitted curve of the signal Monte-Carlo simulation. The PDF used is a sum of Johnson SU and Bukin PDF. Below each fit, the pull plot is shown.

Extracting a PDF for the normalisation channel is more challenging due to the low statistics. In order to overcome this obstacle, a reduced selection procedure including all cuts that alter the shape was implemented (only to extract the PDF and the parameters of the fit. Therefore, the values obtained for the efficiencies are unaffected). This reduced selection includes all trigger cuts (L0, HLT1 and HLT2), as well as particle identification only for muons and truth matching. The PDF chosen in this case is a CrystalBall [20] function (see

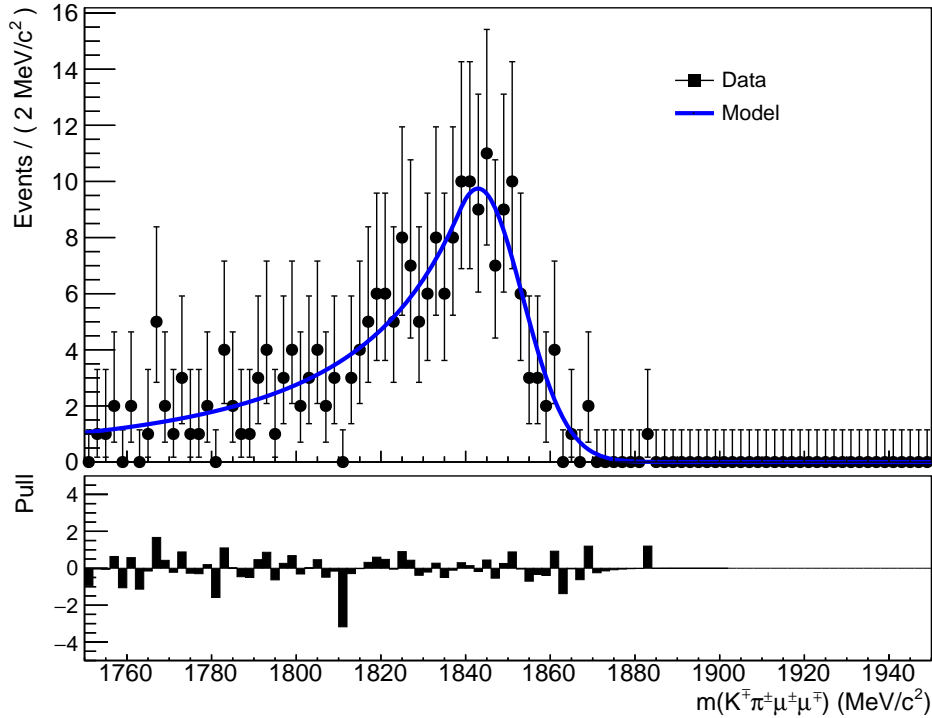
Eq.7) for both cases (with and without dimuon mass range).

$$PDF(CrystalBall) = \begin{cases} \exp\left(-\frac{1}{2} \cdot \left(\frac{x-x_0}{\sigma}\right)^2\right) & \text{if } \frac{x-x_0}{\sigma} \geq -\alpha \\ \left(\frac{n}{|\alpha|}\right)^n \cdot \exp\left(-\frac{|\alpha|^2}{2}\right) \cdot \left(\frac{n}{|\alpha|} - |\alpha| - \frac{x-x_0}{\sigma}\right)^{-n} & \text{if } \frac{x-x_0}{\sigma} < -\alpha \end{cases} \quad (7)$$

where x is the mass variable, x_0 is the average value of the mass, σ represents the width of the Gaussian component and α and n are parameters to be determined by the fit.



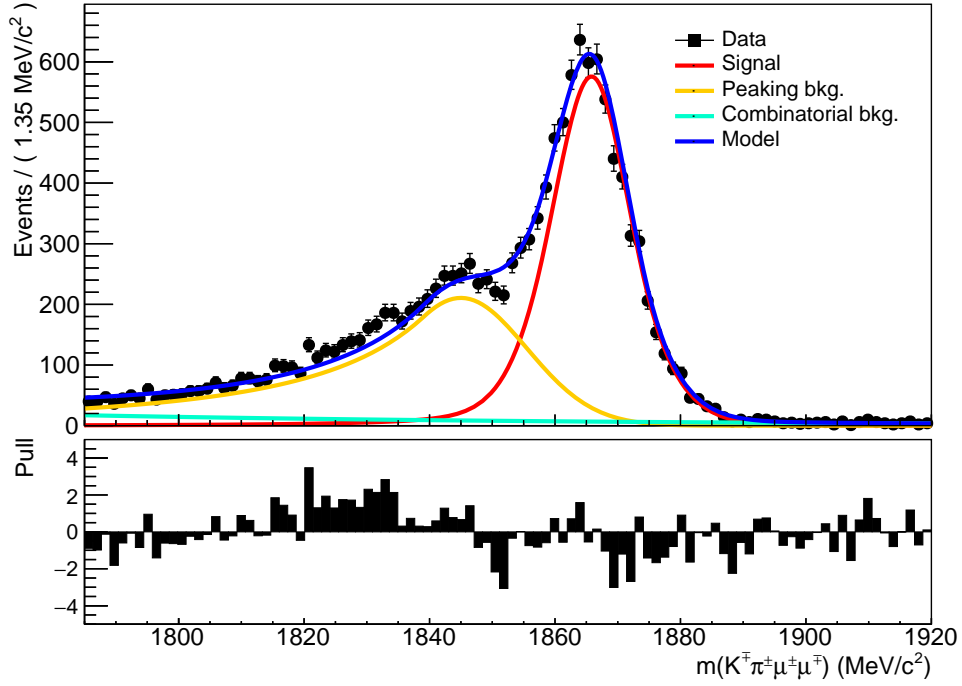
(a) Fit with dimuon mass range cut.



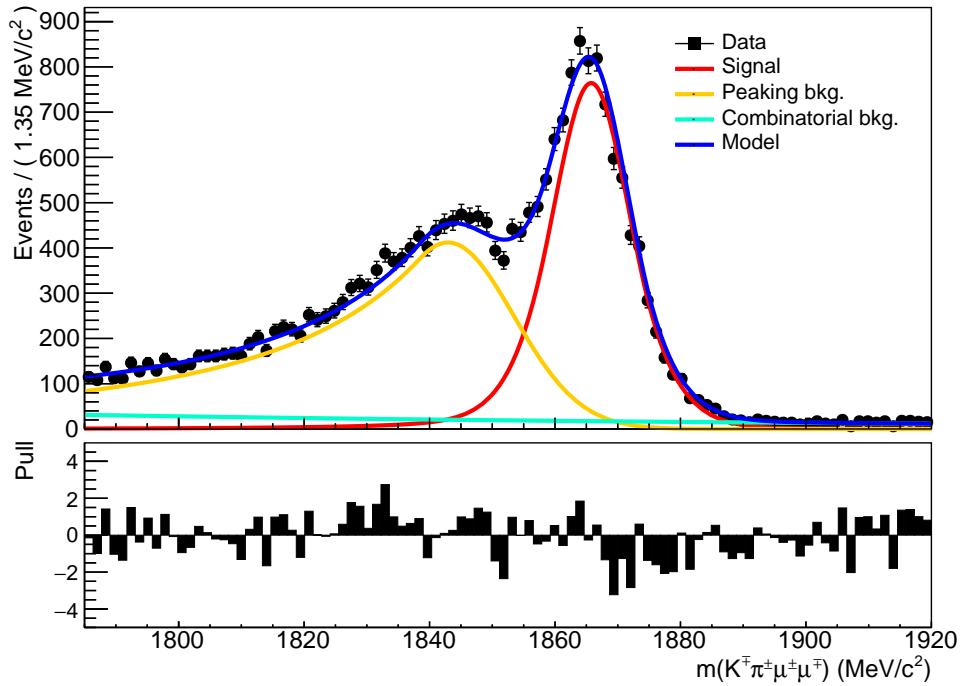
(b) Fit without dimuon mass range cut.

Figure 8: Fitted curve of the normalisation Monte-Carlo simulation. The PDF used is a CrystalBall function. Below each fit, the pull plot is shown.

Figure 8 shows the fitted data samples of $D^0 \rightarrow K^- \pi^+ \pi^+ \pi^-$ with and without dimuon mass range restriction. It must be noted that the number of events fitted is still low, even though the reduced selection procedure has been applied.



(a) Fit with dimuon mass range cut.



(b) Fit without dimuon mass range cut.

Figure 9: Fitted curves of the data samples after a simultaneous fit has been performed. The signal is modelled with a sum of Johnson and Bukin PDFs. The peaking background is described by a CrystalBall PDF, while the combinatorial background follows an exponential curve. Below each fit, the pull plot is shown.

Once the PDF and parameters for signal and normalisation channels are obtained, a fit to the data sample (after the selection procedure is applied) is performed. In order to do so,

the combinatorial background is modelled as an exponential function (see Eq.8).

$$PDF(Exponential) = \exp(\gamma x) \quad (8)$$

where x is the mass and γ is a parameter that is obtained during the fit process.

According to Eq.(1), the magnitudes needed from the fit are the number of signal events ($\mathcal{N}_{D^0 \rightarrow K^- \pi^+ \mu^+ \mu^-}$) and the number of peaking background events ($\mathcal{N}_{D^0 \rightarrow K^- \pi^+ \pi^+ \pi^-}$). The branching ratios of the decays $D^0 \rightarrow K^- \pi^+ \mu^+ \mu^-$ and $D^0 \rightarrow K^- \pi^+ \pi^+ \pi^-$ are obtained in different mass regions ($D^0 \rightarrow K^- \pi^+ \mu^+ \mu^-$ has limited dimuon mass), so two data sets (with and without dimuon mass range restriction) must be considered. The final data sets are simultaneously fitted. In the dimuon data sample, the fit parameters are the number of peaking and combinatorial background candidates. In the data sample without dimuon mass range restriction, the signal and the combinatorial background yields are the fit parameters. Additionally, the branching ratio is a common parameter to both data sets and is determined by the fit. By letting the branching ratio be one of the parameters used in the fit, the value and its corresponding statistical uncertainty are obtained. The result can be seen in Fig. 9. The peak located around 1830 MeV/ c^2 (see Fig. 9a) might be a signature of an additional source of background or some data fluctuation. Table 9 collects the different fit parameters. $\mathcal{N}_{D^0 \rightarrow K^- \pi^+ \mu^+ \mu^-}$ (dimuon) and $\mathcal{N}_{D^0 \rightarrow K^- \pi^+ \pi^+ \pi^-}$ (no dimuon) have been obtained following Eq. (1).

	Parameter	Value (dimuon)	Value (no dimuon)
Signal Monte-Carlo	μ	1867±10	1866.7±0.7
	λ	5.8±0.7	6.0±1.9
	γ	0.6±6.5	0.57±0.06
	δ	0.8±0.3	0.81±0.04
	x_p	1866±48	1866.0±0.1
	σ_p	7±16	6.42±0.06
	x_i	$(0.0007 \pm 2.1882) \times 10^{-4}$	$(0.08 \pm 4.84) \times 10^{-3}$
	ρ_1	-0.4±0.6	-0.31±0.07
	ρ_2	-0.2±0.6	-0.20±0.03
	c	0.20±0.17	0.17±0.03
Normalisation Monte-Carlo	x_0	1845±1	1843±1
	σ	10.5±0.5	10.5±0.6
	α	0.6±0.3	0.4±0.2
	n	2.2±2.4	2.3±2.3
Data	$\mathcal{N}_{D^0 \rightarrow K^- \pi^+ \mu^+ \mu^-}$	7369±858	9813±103
	$\mathcal{N}_{D^0 \rightarrow K^- \pi^+ \pi^+ \pi^-}$	5826±84	7758±931
	$\mathcal{N}_{combinatorial}$	872±77	1983±143

Table 9: Fit parameters and their uncertainties. The values have been obtained for the two data sets studied (with and without dimuon mass restriction).

5.1 Branching ratio

The procedure described previously yields a value of the branching ratio of:

$$\mathcal{BR} = (5.70 \pm 0.09) \times 10^{-6}$$

where the uncertainty is statistical, which is directly obtained from the simultaneous fit and is a result of the fluctuations inherent to the fit.

According to the systematic uncertainty's study done in [10], the systematic uncertainty has different sources. These are uncertainties in the reconstruction of the decay, which include track reconstruction, offline selection, simulated decay models, hardware and software trigger, muon and kaon identification and size of the simulated sample. In this thesis, the uncertainty stemming from the efficiencies represents only the uncertainty of the size of the simulated sample. In order to obtain a value for the systematic uncertainty of the efficiencies, more studies should be done but there is no apparent reason that suggests that the previously studied in [10] systematic uncertainties would vanish.

Source	Uncertainty (%)
Track reconstruction	-
Offline selection	-
Simulated decay models	-
Hardware trigger	-
Software trigger	-
Muon identification	-
Kaon identification	-
Size of simulated sample	7.05
Signal shape parameter	-
Peaking background tails	-
Signal PDF	-
Non-peaking background shape	-
$\mathcal{BR}(D^0 \rightarrow K^- \pi^+ \mu^+ \mu^-)$	1.95
Quadratic sum	7.37

Table 10: Systematic uncertainties on $\mathcal{BR}(D^0 \rightarrow K^- \pi^+ \mu^+ \mu^-)$. The hyphen represents that the source has not been studied in this thesis.

Another source of systematic uncertainty is the fit model. A full analysis of this uncertainty would involve the generation of fake data to check for possible biases in the fit. Different PDFs should also be used to estimate the impact of the PDF on the final result. For instance, the combinatorial background could be modelled as a linear function. The last source of systematic uncertainty is the uncertainty of the branching ratio of the normalisation

channel. A summary of the systematic uncertainties studied in the last measurement of $D^0 \rightarrow K^- \pi^+ \mu^+ \mu^-$ with the LHCb as well as the values obtained in this thesis can be seen in Table 10.

The efficiency ratio is the main source of systematic uncertainty. It could be reduced if the size of the simulation sample for the decay $D^0 \rightarrow K^- \pi^+ \pi^+ \pi^-$ was bigger. The systematic uncertainty must be larger than 0.42×10^{-6} , which is obtained by summing in quadrature, as no correlation between them is assumed.

6 Conclusions

A measurement of the branching fraction of $D^0 \rightarrow K^- \pi^+ \mu^+ \mu^-$ is presented in this thesis. Data collected with the LHCb detector in the years 2017 and 2018 with an integrated luminosity of 3.8 fb^{-1} and at a centre of mass energy of 13 TeV are analysed. The value of the branching fraction is measured to be:

$$\mathcal{BR} = (5.70 \pm 0.09 \text{ (stat.)} \pm 0.42 \text{ (syst.)}) \times 10^{-6}$$

where the uncertainties are statistical and systematic, respectively. The systematic uncertainty is an underestimation of the value, as it only includes the effect of the normalisation branching ratio and the size of the simulation sample.

The measurement is within 2.6σ to the value obtained with the LHCb for the resonant spectrum (see table 5). Additionally, it can be seen that it is below the upper limit for the same decay reported by the E791 collaboration. It can also be compared to the theoretical prediction for the full dimuon mass range (see Table 5). The obtained value is below the theoretical prediction, which is in good agreement with the fact that the obtained value is for the resonant spectrum only.

The following step in the analysis of the decay would be to further study the impact of the fit on the final value of the branching ratio by producing fake data to check if the fit produces an unbiased result. This step would have a direct impact on the systematic uncertainty. However, this was outside the scope of this thesis.

A more complete study of the systematic uncertainty would include a deeper analysis of the normalisation channel efficiencies, as they are obtained from simulations where the pions were reconstructed as muons, reducing the available simulation data significantly. The production of simulation data to estimate them requires a long period of time and a large amount of resources and was, therefore, discarded. Comparing the uncertainty due to the size of the normalisation channel sample with the systematic uncertainty of the previous measurement performed by the LHCb shows that the simulation sample is the main limiting factor of this measurement. Systematic uncertainties affecting the measured signal yield were not studied.

Summarising, more systematic cross checks are needed to validate the value for the branching fraction obtained in this thesis.

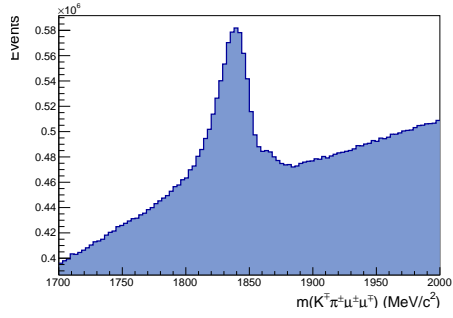
References

- [1] H. Gisbert, M. Golz, and D. S. Mitzel, “Theoretical and experimental status of rare charm decays,” *Modern Physics Letters A*, vol. 36, no. 04, p. 2130002, 2021.
- [2] M. Thomson, *Modern particle physics*. Cambridge University Press, 2013.
- [3] “Observation of D^0 meson decays to $\pi^+\pi^-\mu^+\mu^-$ and $K^+K^-\mu^+\mu^-$ final states,”
- [4] J. Lees, V. Poireau, V. Tisserand, E. Grauges, A. Palano, G. Eigen, D. Brown, Y. G. Kolomensky, M. Fritsch, H. Koch, *et al.*, “Search for lepton-flavor-violating decays $D^0 \rightarrow X^0 e^\pm \mu^\mp$,” *Physical Review D*, vol. 101, no. 11, p. 112003, 2020.
- [5] M. Aker, A. Beglarian, J. Behrens, A. Berlev, U. Besserer, B. Bieringer, F. Block, S. Bobien, M. Böttcher, B. Bornschein, *et al.*, “Direct neutrino-mass measurement with sub-electronvolt sensitivity,” *Nature Physics*, vol. 18, no. 2, 2022.
- [6] P. Zyla *et al.*, “Review of Particle Physics,” *PTEP*, vol. 2020, no. 8, p. 083C01, 2020. and 2021 update.
- [7] S. Stone, “Pentaquarks and tetraquarks at LHCb,” *arXiv:1509.04051*, 2015.
- [8] G. Bonvicini, D. Cinabro, M. Smith, P. Zhou, P. Naik, J. Rademacker, K. Edwards, R. Briere, H. Vogel, J. Rosner, *et al.*, “Updated measurements of absolute D^+ and D^0 hadronic branching fractions and $\sigma(e^+e^- \rightarrow D\bar{D})$ at $E_{CM}=3774$ MeV,” *Physical Review D*, vol. 89, no. 7, p. 072002, 2014.
- [9] L. Cappiello, O. Cata, and G. D’Ambrosio, “Standard model prediction and new physics tests for $D^0 \rightarrow h^+h^-l^+l^-$ ($h = \pi, K; l = e, \mu$),” *Journal of High Energy Physics*, vol. 2013, no. 4, pp. 1–31, 2013.
- [10] LHCb Collaboration, R. Aaij, *et al.*, “First observation of the decay $D^0 \rightarrow K^- \pi^+ \mu^+ \mu^-$ in the ρ^0 - ω region of the dimuon mass spectrum,” *Physics Letters B*, vol. 757, pp. 558–567, 2016.
- [11] E. Aitala, S. Amato, J. Anjos, J. Appel, D. Ashery, S. Banerjee, I. Bediaga, G. Blaylock, S. Bracker, P. Burchat, *et al.*, “Search for rare and forbidden charm meson decays $D^0 \rightarrow V l^+ l^-$ and $h h l l$,” *Physical Review Letters*, vol. 86, no. 18, p. 3969, 2001.
- [12] I. Belyaev, G. Carboni, N. Harnew, C. Matteuzzi, and F. Teubert, “The history of LHCb,” *The European Physical Journal H*, vol. 46, mar 2021.
- [13] D. Francesca, “LHCb detector and trigger performance in Run II,” in *EPJ Web of Conferences*, vol. 164, p. 01016, EDP Sciences, 2017.
- [14] Y. Amhis, W. Bonivento, A. Contu, O. Kochebina, and B. Viaud, “Measurement of the partial branching ratio of the $D^0 \rightarrow K^- \pi^+ \mu^+ \mu^-$ decay in the ρ/ω region of $m(\mu^+ \mu^-)$,”
- [15] D. Mitzel, *Search for new physics in rare four-body charm decays*. PhD thesis, Heidelberg University, 2019.

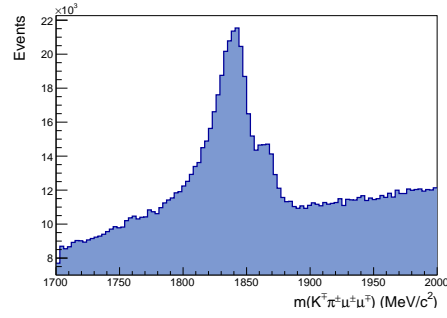
- [16] W. Verkerke and D. P. Kirkby, “The RooFit toolkit for data modeling,” *eConf*, vol. C0303241, p. MOLT007, 2003.
- [17] R. Brun and F. Rademakers, “ROOT—An object oriented data analysis framework,” *Nuclear instruments and methods in physics research section A: accelerators, spectrometers, detectors and associated equipment*, vol. 389, no. 1-2, pp. 81–86, 1997.
- [18] A. Bevan and F. Wilson, “Afit user guide,” *Tech. Rep.*, 2010.
- [19] N. L. Johnson, “Systems of frequency curves generated by methods of translation,” *Biometrika*, vol. 36, no. 1/2, pp. 149–176, 1949.
- [20] S. Das, “A simple alternative to the Crystal Ball function,” *arXiv:1603.08591*, 2016.

A Evolution of the events sample with the different cuts

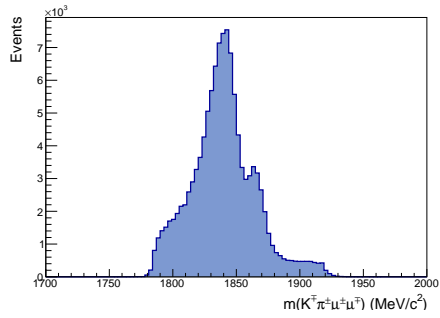
A.1 Data sample



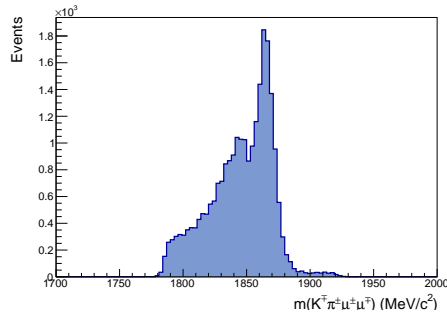
(a) Data sample before any cut was applied.



(b) Data sample after trigger cuts.

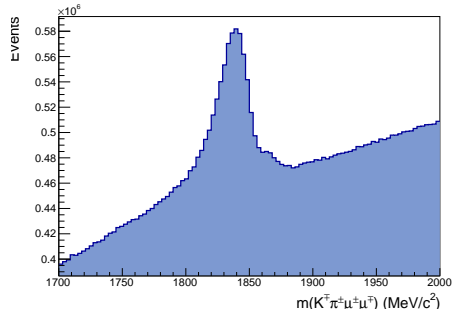


(c) Data sample after selection cuts.

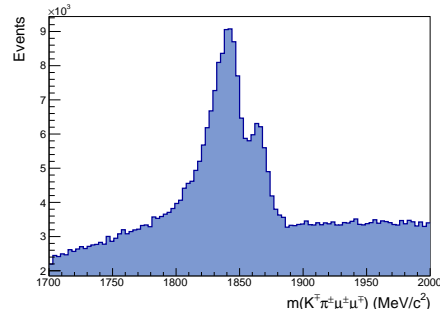


(d) Data sample after all cuts are applied.

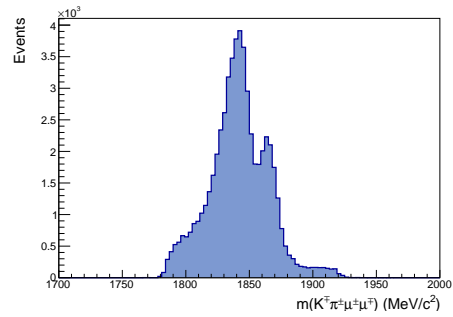
Figure 10: Evolution of the data sample (**without dimuon mass range**) after selection cuts are applied.



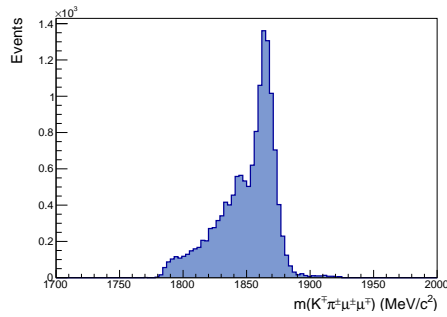
(a) Data sample before any cut was applied.



(b) Data sample after trigger cuts.



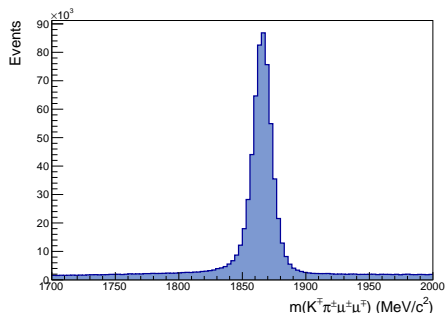
(c) Data sample after selection cuts.



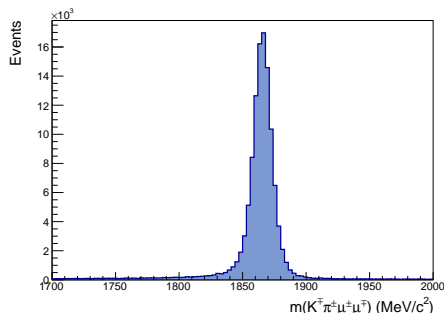
(d) Data sample after all cuts are applied.

Figure 11: Evolution of the data sample (**with dimuon mass range**) after selection cuts are applied.

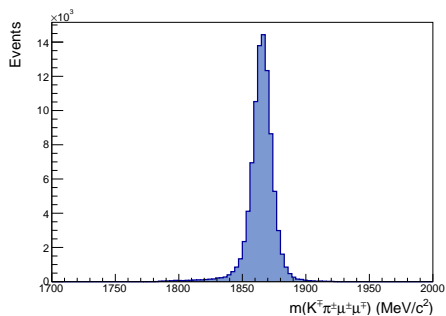
A.2 Signal simulation sample



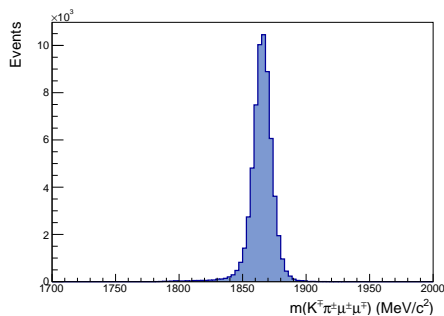
(a) Signal sample before any cut was applied.



(b) Signal sample after trigger cuts.

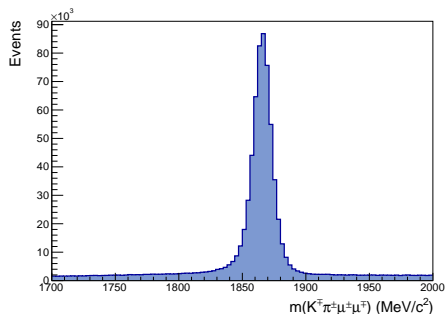


(c) Signal sample after selection cuts.

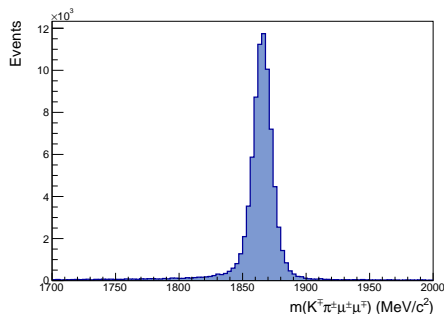


(d) Signal sample after all cuts are applied.

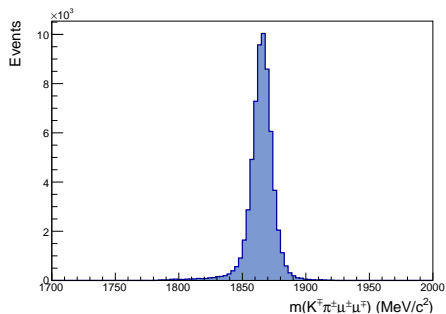
Figure 12: Evolution of the signal simulation sample (**without dimuon mass range**) after selection cuts are applied.



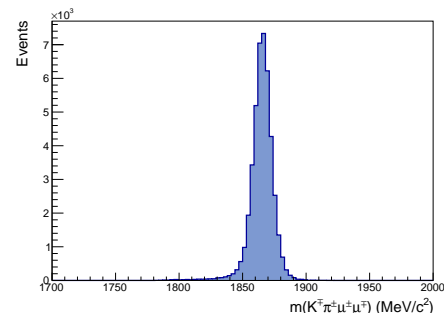
(a) Signal sample before any cut was applied.



(b) Signal sample after trigger cuts.



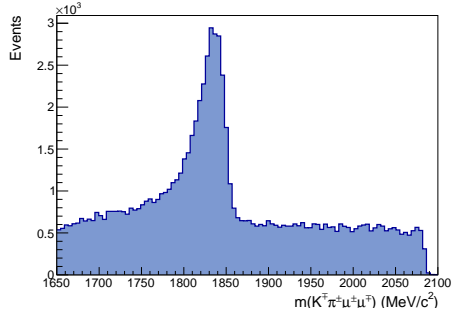
(c) Signal sample after selection cuts.



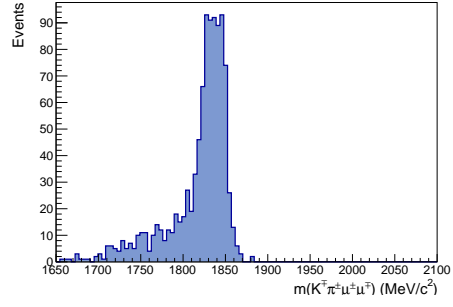
(d) Signal sample after all cuts are applied.

Figure 13: Evolution of the signal simulation sample (**with dimuon mass range**) after selection cuts are applied.

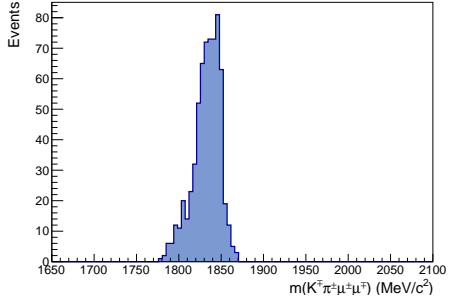
A.3 Normalisation simulation sample



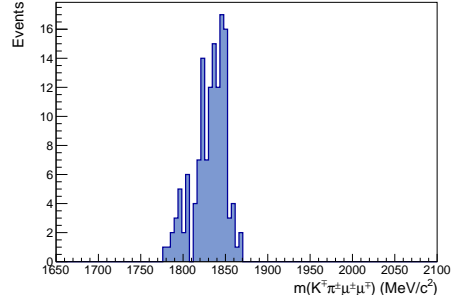
(a) Norm. sample before any cut was applied.



(b) Normalisation sample after trigger cuts.

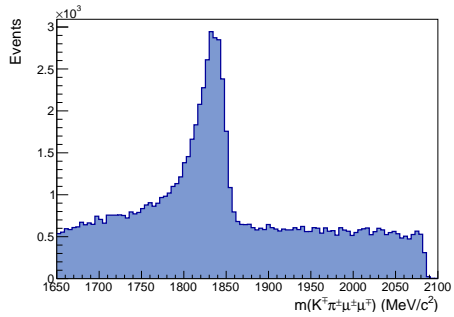


(c) Normalisation sample after selection cuts.

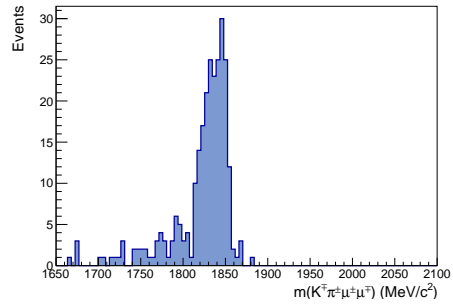


(d) Normalisation sample after all cuts are applied.

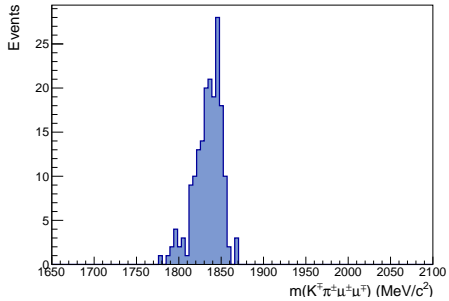
Figure 14: Evolution of the normalisation simulation sample (**without dimuon mass range**) after selection cuts are applied.



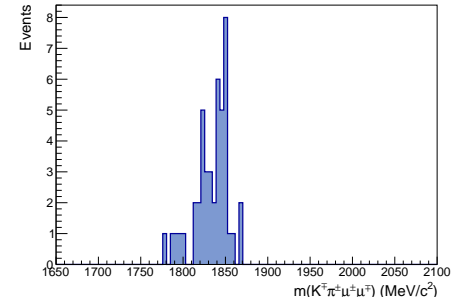
(a) Norm. sample before any cut was applied.



(b) Normalisation sample after trigger cuts.



(c) Normalisation sample after selection cuts.



(d) Normalisation sample after all cuts are applied.

Figure 15: Evolution of the normalisation simulation sample (**with dimuon mass range**) after selection cuts are applied.

List of Figures

1	Schematic diagram of $D^{*+} \rightarrow D^0(\rightarrow K^- \pi^+ \mu^+ \mu^-) \pi^+_s$	4
2	LHCb detector.	7
3	Trigger overview.	9
4	Data sample before and after selection procedure.	14
5	Signal simulation sample before and after selection procedure.	15
6	Normalisation simulation sample before and after selection procedure.	16
7	Signal fit.	20
8	Normalisation channel fit.	21
9	Data fit.	22
10	Data sample before and after selection procedure without dimuon mass range restriction.	29
11	Data sample before and after selection procedure with dimuon mass range restriction.	29
12	Signal simulation sample before and after selection procedure without dimuon mass range restriction.	30
13	Signal simulation sample before and after selection procedure with dimuon mass range restriction.	30
14	Normalisation simulation sample before and after selection procedure without dimuon mass range restriction.	31
15	Normalisation simulation sample before and after selection procedure with dimuon mass range restriction.	31

List of Tables

1	Quarks in the Standard Model.	2
2	Leptons in the Standard Model.	3
3	Gauge bosons in the Standard Model.	3
4	Properties of the mesons studied.	3
5	Theoretical and experimental value for the \mathcal{BR}	6
6	Number of events in studied samples	11
7	Selection criteria.	13
8	Efficiencies.	18
9	Fit parameters.	23
10	Systematic uncertainties on $\mathcal{BR}(D^0 \rightarrow K^- \pi^+ \mu^+ \mu^-)$	24

Acknowledgement

First of all, I would like to thank my supervisor Prof. Dr. Ulrich Uwer for giving me the opportunity to work in the LHCb group in Heidelberg and helping me with all the additional procedures as an exchange student. I am also thankful to Dr. Juan Terrón for agreeing to be the second supervisor. I am deeply indebted to MSc. Daniel Unverzagt for guiding me through my research and answering my questions.

I would like to extend my sincere thanks to my friends, both in Spain (Lord Kelvin, we did it!) and in Germany.

Por último, quiero dar las gracias a mis padres: Francisca y Santiago. Gracias por apoyarme en todos mis proyectos y locuras, por nunca ponerme límites y por enseñarme que, en esta vida, nunca hay que rendirse. Obrigada.